



Article

New Electrospun Polystyrene/Al₂O₃ Nanocomposite Superhydrophobic Coatings; Synthesis, Characterization, and Application

Ahmed Bahgat Radwan ¹, Aboubakr M. Abdullah ^{1,*} , Adel M. A. Mohamed ^{2,3}  and Mariam A. Al-Maadeed ¹

¹ Center for Advanced Materials, Qatar University, Doha 2713, Qatar; ahmedbahgat@qu.edu.qa (A.B.R.); m.alali@qu.edu.qa (M.A.A.-M.)

² Département des Sciences Appliquées, Université du Québec à Chicoutimi, Chicoutimi, QC G7H 2B1, Canada; adel.mohamed25@yahoo.com

³ Department of Metallurgical and Materials Engineering, Faculty of Petroleum and Mining Engineering, Suez University, Suez 43721, Egypt

* Correspondence: bakr@qu.edu.qa; Tel.: +974-3307-0591

Received: 20 December 2017; Accepted: 1 February 2018; Published: 8 February 2018

Abstract: The effect of electrospinning operational parameters on the morphology, surface roughness, and wettability of different compositions of electrospun polystyrene (PS)–aluminum oxide (Al₂O₃) nanocomposite coatings was investigated using different techniques. For example, a scanning electron microscope (SEM) coupled with an energy dispersive X-ray (EDX) unit, a Fourier transform infrared (FTIR) spectrometer, an atomic force microscope (AFM), and water contact angle (WCA), and contact angle hysteresis (CAH) measurements using the sessile droplet method, were used. The latter used 4 μL of distilled water at room temperature. PS/Al₂O₃ nanocomposite coatings exhibited different morphologies, such as beaded fibers and microfibers, depending on the concentration ratio between the PS and Al₂O₃ nanoparticles and the operational parameters of the electrospinning process. The optimum conditions to produce a nanocomposite coating with the highest roughness and superhydrophobic properties (155° ± 1.9° for WCA and 3° ± 4.2° for CAH) are 2.5 and 0.25 wt % of PS and Al₂O₃, respectively, 25 kV for the applied potential and 1.5 mL·h^{−1} for the solution flow rate at 35 °C. The corrosion resistance of the as-prepared coatings was investigated using the electrochemical impedance spectroscopy (EIS) technique. The results have revealed that the highly porous superhydrophobic nanocomposite coatings (SHCs) possess a superior corrosion resistance that is higher than the uncoated Al alloy by three orders of magnitude.

Keywords: electrospinning; polystyrene; aluminum oxide; nanocomposite; coating; superhydrophobic; morphology; surface roughness

1. Introduction

Superhydrophobic surfaces with low sliding angle (SA ≤ 10°) and high water contact angle (WCA ≥ 150°) exhibit a low resistance to water mobility on the surface as a result of the embedded air in the composite under the water on these surfaces [1,2]. Such surfaces have attracted a significant interest because of their potential applications in many industrial fields and biological processes, e.g., highly corrosion resistant [3] and anti-adhesive coatings [4], self-cleaning materials [5], antifingerprint optical devices [6], printing technologies [7], water–oil separation [8], and digital microfluidics [9].

Many examples of natural superhydrophobic materials exist, e.g., the lotus leaf, which is equipped with hierarchical surface projections, insect wings, and animal fur [10–14]. The

superhydrophobic behavior is usually attributed to a combination of a hydrophobic surface and micro or nanostructures.

Synthetic superhydrophobic surfaces have been synthesized in the last decades in which the surface chemistry and roughness were tailored to decrease the surface energy and maintain trapped air at the material-water interface. The synthesis was achieved using different methods, e.g., microfabrication and chemical processes [15–18]. In 1943, a superhydrophobic material was fabricated using electrospinning [19], which is a technique that uses a high electric field to produce fibers from solutions of polymeric materials. The properties of these solutions, such as the surface tension, the viscosity, and the molecular weight of the polymer, in addition to the electrospinning parameters, e.g., the distance between a needle and a substrate, the solution flow rate, and the applied voltage, are the main factors that influence the electrospinning process that affects the properties of the produced fibers. Consequently, the optimum conditions of the electrospinning process for numerous polymers were studied [20–24]. It is worth mentioning that the advantage of the electrospinning technique compared to other ones, e.g., drawing [25] template synthesis [26], phase separation [27], and self-assembly [28], is the ability to develop it for mass production, simplicity, and inexpensiveness. In addition, it can be used for a wide range of polymers to create nanofibers [29–32].

Polystyrene (PS) is a glassy and amorphous polymer that is commonly rigid and relatively cheap. It is a poor barrier to oxygen and water vapor and has a relatively low melting point [33]. PS is currently used in several applications, e.g., packaging, electrical/electronic applications, toys, sheets, household goods, insulation, etc. It should be mentioned that selecting the solvent in the electrospinning of PS is a critical issue. A systematic analysis was conducted for eighteen various solvents to find the most suitable one for PS electrospinning. It was concluded that *N,N*-dimethylacetamide (DMAc) and tetrahydrofuran (THF) are the best candidates [34].

Acatay et al. studied the relationship between the surface morphology and the degree of superhydrophobicity of a material [35]. The fabrication of a superhydrophobic PS by the addition of inorganic nanomaterials such as SiO₂ [36], TiO₂ [37], and MnO₂ [38] has been studied. The addition of these nanoparticles led to an increase in the surface roughness and a decrease in the surface energy of the PS–oxide nanoparticles composite coating in addition to enhancing the formation of hierarchical shapes [39]. Electrospun PS/Al₂O₃ nanocomposite is also expected to have, at least, the same superhydrophobic nature as the PS/SiO₂, TiO₂, or MnO₂ with better physical properties, e.g., transparency and stability, insulation and hardness [40]. Furthermore, its high corrosion resistance can be exploited in many applications, e.g., protective coating, fire retarder, insulators, and catalysis [41]. Therefore, the target of this work is studying the effect of the compositional ratio between the PS and the Al₂O₃ nanoparticles in addition to the electrospinning operational parameters on the superhydrophobic behavior of the nanocomposite coatings on Al substrates. Moreover, the protection of the fabricated superhydrophobic coatings (SHCs) against corrosion is studied in saline water.

2. Materials and Methods

Commercial aluminum foil was used as a substrate for the experiments. PS with a molecular weight of 250 kDa was purchased from Sigma-Aldrich (Taufkirchen, Germany). DMAc and THF, obtained from BDH Chemicals (Doha, Qatar), were used as nonvolatile and volatile solvents, respectively. Al₂O₃ nanoparticles of a size <20 nm were used to enhance the hydrophobicity of PS based-polymer matrix (Sigma-Aldrich, Taufkirchen, Germany).

Different amounts of PS were dissolved in a mixture of 70 wt % DMAc and 30 wt % THF at 35 °C for 12 h and stirred until getting a sufficiently viscous solution that is required for electrospinning. In-parallel, different concentrations of Al₂O₃ nanoparticles were dispersed in DMAc/THF mixtures of the same ratio under vigorous stirring conditions until a homogenous dispersion of the nanoparticles was obtained. The dispersed Al₂O₃ nanoparticles in DMAc/THF were then added to the PS solution to achieve the desired weight ratio of Al₂O₃ to PS. The different PS and Al₂O₃ concentrations used in this study are shown in Table 1.

Table 1. Compositional ratios and electrospinning operational parameters for pure PS and PS/Al₂O₃ nanocomposite coatings.

Exp. Code	PS (wt %)	Al ₂ O ₃ (wt %)	Potential (kV)	Flow Rate (mL·h ⁻¹)
PS1	2.5	–	20	1.5
PS2	2.5	–	25	2
PS3	2.5	–	25	1.5
PS4	5	–	25	1.5
PA1	2.5	0.25	20	1.5
PA2	2.5	0.35	25	2
PA3	2.5	0.25	25	1.5
PA4	5	0.25	25	1.5

Prior to electrospinning, aluminum substrates (which will be used as a collector) were mechanically polished using Grinder polisher (Metko FORCIPO1V, Bursa, Turkey), degreased ultrasonically for 30 min, and cleaned by distilled water and finally dried. An electrospinning unit consisting of a syringe pump, a high voltage supply, and a collector was used. Syringe pump was aligned horizontally, and electric field was maintained by the high voltage power supply. The complex solutions were stored in syringes behind the needles. The distance between the tip of the needle and the collector was 15 cm. The electrospinning of the nanocomposite solutions was performed using a needle with an inside diameter of 0.25 mm at flow rates of 1.5 and 2 mL·h⁻¹ and an applied voltage of 20 and 25 kV, while the operating temperature was kept constant at 35 °C. After the electrospinning process, nanofibers were dried overnight.

Characterization Techniques

High field emission scanning electron microscopy, HFSEM, (FEI NOVA NANOSEM 450, Hillsboro, OR, USA) coupled with an energy dispersive X-ray unit, EDX, was used to investigate the morphology of the fabricated nanocomposite coatings. For water contact angle data, a 4 µL water droplet was placed onto the different coating surfaces using OCA 35 Contact Angle Measuring System (Dataphysics Instruments, Filderstadt, Germany). The sliding angle (SA) was measured by tilting the substrate until the droplet was noticed to move and the advancing (largest) contact angle (ACA) and receding (smallest) contact angle (RCA) were recorded. The initial water contact angles were measured at 5 different locations at the surface of each specimen. Fourier transform infrared spectroscopy (FTIR) spectra were recorded in a range of 4000–400 cm⁻¹ using PerkinElmer Spectrum 400 FTIR, PerkinElmer, Waltham, MA, USA. Atomic force microscopy (AFM) analysis was carried out using an MFP-3D, Asylum Research, Santa Barbara, CA, USA. AFM was performed using a silicon tip with a radius of 10 nm and a resonance frequency of 70 kHz besides a spring constant of 2 Nm⁻¹ in the non-contact tapping mode in air. Electrochemical impedance spectroscopy (EIS) measurements were performed using a Gamry Reference 3000 potentiostat, Warminster, PA, USA, in 3.5 wt % NaCl solutions within a frequency range of 0.01 Hz to 100 kHz with a wave amplitude of 5 mV at 25 °C. EIS data analysis was performed using a Gamry Echem Analyst software (Version 7.06, Gamry, Warminster, PA, USA). Before running any EIS experiment, the samples were immersed in the 3.5 wt % NaCl electrolyte for 30 min.

3. Results and Discussion

3.1. Surface Morphology of the Coatings

The representative SEM micrographs of the electrospun PS with different concentrations of Al₂O₃ nanoparticles are shown in Figures 1 and 2, respectively. Different morphologies of PS in absence and presence of Al₂O₃ nanoparticles including beaded fibers and free beads are obtained by varying the concentration of PS and Al₂O₃ and/or the operational parameters of the electrospinning process.

Table 2 shows the average nanofiber diameter of the different prepared coatings before and after the addition of Al_2O_3 nanoparticles.

Table 2. The average diameter of the nanofibers and beads of PS and PS/ Al_2O_3 nanocomposite coatings.

PS Codes	Average Fiber Diameter (nm)	PA Codes (PS/ Al_2O_3)	Average Fiber Diameter (nm)
PS1	340 \pm 27	PA1	325 \pm 23
PS2	328 \pm 29	PA2	315 \pm 27
PS3	320 \pm 21	PA3	290 \pm 34
PS4	433 \pm 15	PA4	413 \pm 21

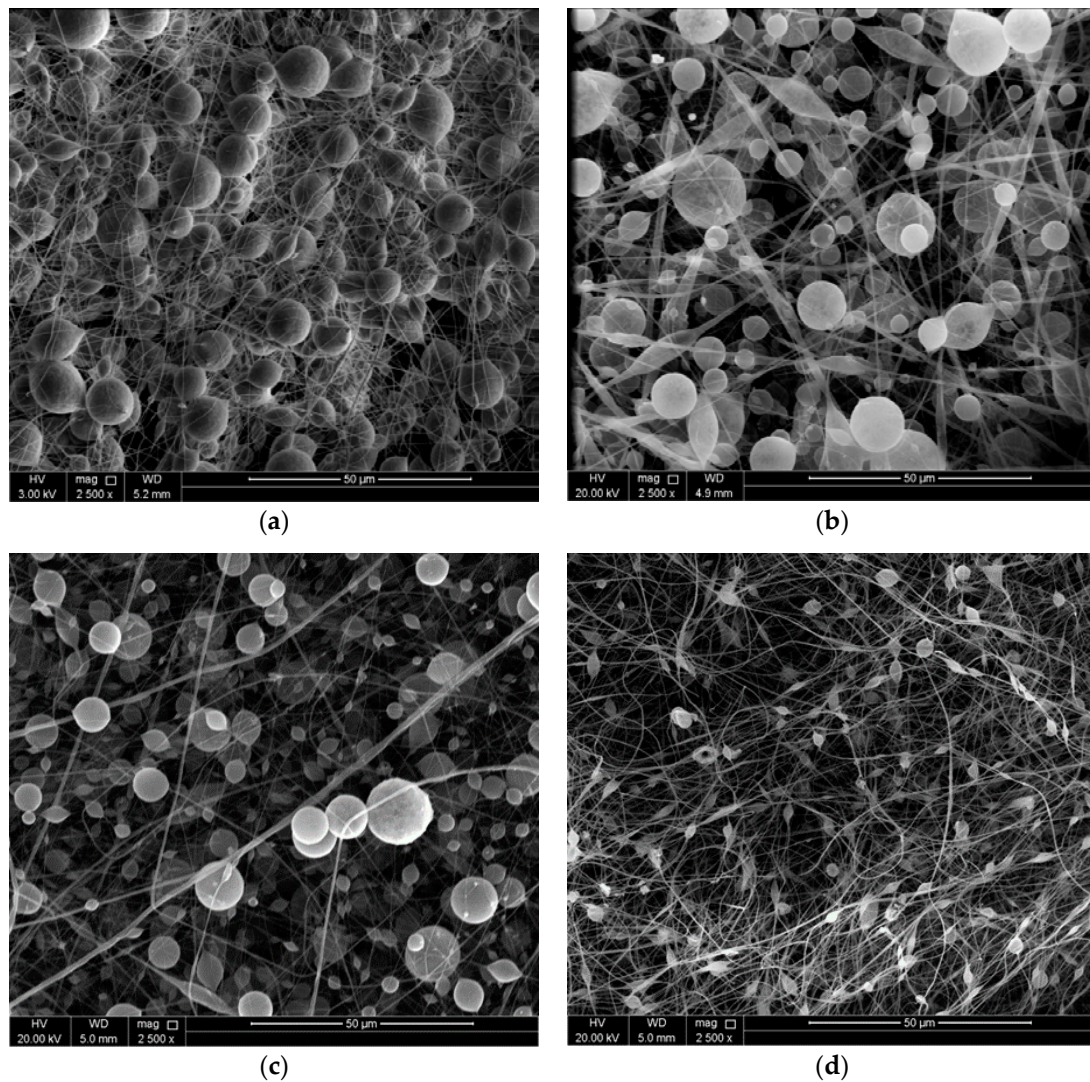


Figure 1. SEM micrographs of the as prepared PS coating without any addition of Al_2O_3 nanoparticles for (a) PS1, (b) PS2, (c) PS3, and (d) PS4 (See Table 1 for the operational parameters).

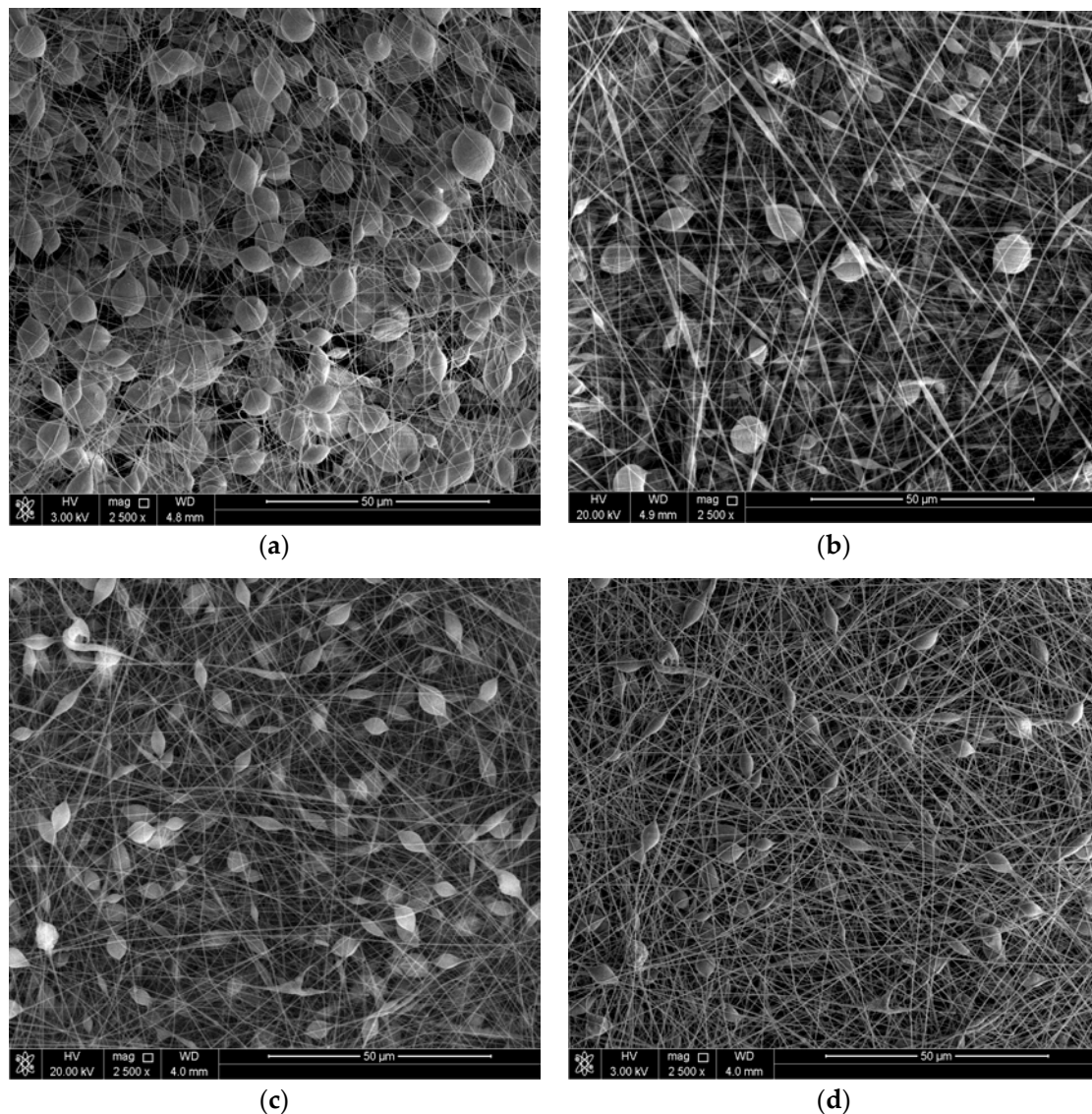


Figure 2. The SEM images of PS/ Al_2O_3 nanocomposite coating for (a) PA1, (b) PA2, (c) PA3, and (d) PA4 (See Table 1 for Operational parameters).

The morphologies of the pure PS polymer shown in Figure 1 reveal the formation of a beaded-fiber structure. At low applied voltages, the bead shape is spindle-like, Figure 1a,b. However, increasing the applied voltage and/or the PS concentration leads to a decrease in the number of beads and changes them to a spherical-like shape, Figure 1c,d, due to the increase of the jet stretching. The bead formation can be demonstrated by the insufficient swift stretching through the flagellation of the jet [42]. This observation is inconsistent with the previous work [34]. Moreover, at low PS concentration, the elasticity is too small to supply enough resistance to tolerate the stretching, which results from the electrostatic force, leading to the formation of a large number of beads. However, by increasing the PS concentration from 2.5 to 5 wt %, the ultrafine PS fibers are formed with a small number of beads per unit area, demonstrating that the elastic properties of PS solution are more significant at high concentrations, as shown in Figure 1d.

The SEM micrographs shown in Figure 2 display the effect of adding Al_2O_3 nanoparticles on the surface morphology of an electrospun PS polymer. The SEM micrographs show the formation of different sizes of beaded fibers without a significant change in the surface morphology.

Table 2 shows a significant variation in the fiber diameter as the concentrations of PS polymer and Al_2O_3 nanoparticles, as well as the electrospinning parameters, change. It can be observed that the increase in the applied voltage from 20 to 25 kV, while other parameters are kept constant, leads to a decrease in the average nanofiber diameters of PS1 and PS3 to 340 ± 27 and 320 ± 21 nm, respectively. Increasing the applied voltage results in a large elongation of the solution owing to the greater columbic forces in the jet, in addition to the high electric field, which leads to the formation of thinner fibers [43,44]. However, as the concentration of PS is increased from 2.5 g (PS3) to 5 g (PS4), the average nanofiber diameter is increased from 320 ± 21 to 433 ± 15 nm, respectively.

The higher the quantity of polymer chains in the solution, the easier the capability of the electrospinning jet to elongate the solution, while the solvent molecules are dispersed between the polymer chains [21,34,45]. In addition, with an increase of the wt % of PS, the increased viscoelastic force can hinder the jet segment from being stretched by the constant columbic force, yielding fibers with large diameters [34]. On the other hand, it was found that the fiber diameter of PS2 and PS3 diminished to 328 ± 29 nm and 320 ± 21 nm, respectively, by reducing the flow rate from 2 to $1.5 \text{ mL}\cdot\text{h}^{-1}$. By increasing the flow rate, the quantity of polymer flowing through the tip of the needle increases, which in turn produces thick fibers. Moreover, at very high flow rates, the polymeric jet was unsettled and tended to electrospray owing to the influence of the gravitational force.

Table 2 shows the formation of fibers with different diameters after the addition of Al_2O_3 nanoparticles to the solutions with different PS concentration. It worth mentioning that addition of Al_2O_3 nanoparticles leads to a significant decrease in the diameter of the fibers in comparison with the pure PS. However, further addition of alumina nanoparticles decreases the fiber diameter from 320 ± 21 of PS3 to 290 ± 34 nm of PA3. These results are inconsistent with a previous report [46].

Figure 3a,b shows the SEM/EDX mapping of PA1 and PA3 SHCs, which verifies the presence and the uniform dispersion of the alumina nanoparticles on the beaded fiber structure.

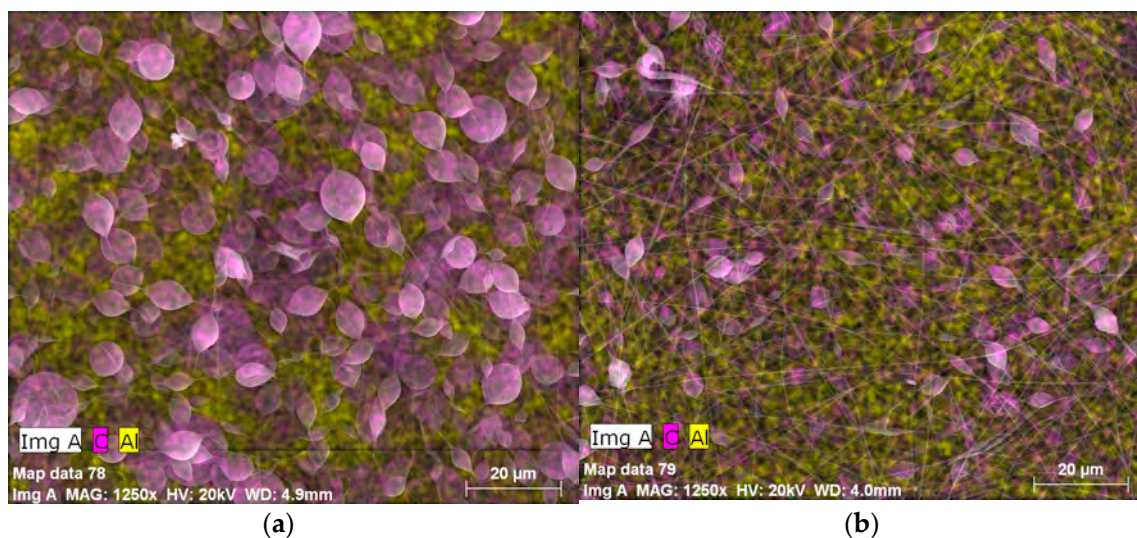


Figure 3. The SEM/EDX mapping micrographs of the as-prepared SHCs (a) PA1 and (b) PA3.

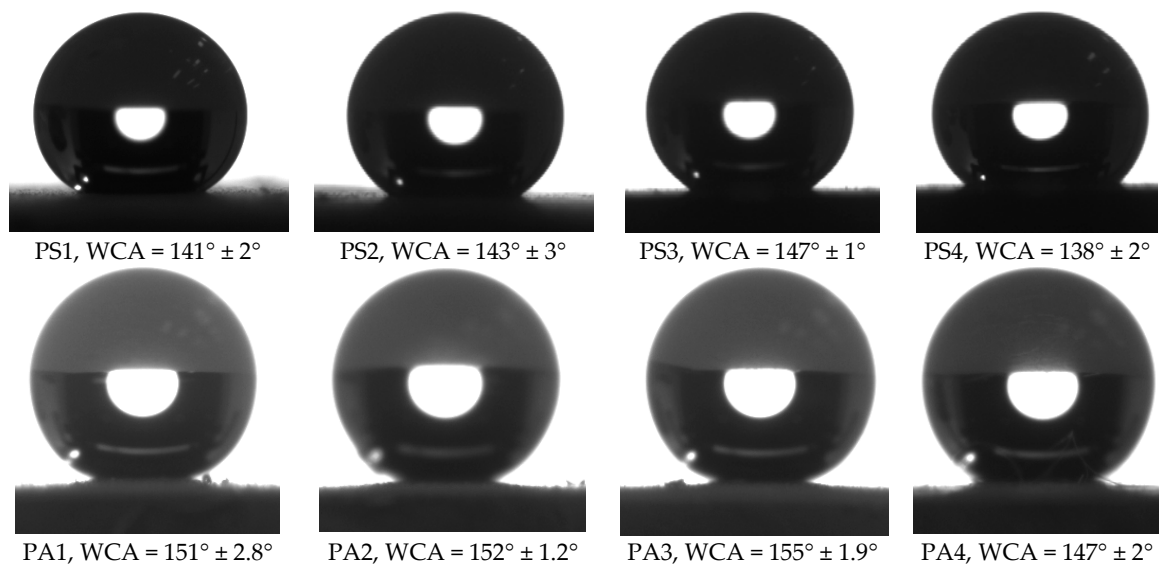
3.2. Wettability

The effect of changing the compositional ratio between PS and Al_2O_3 and the different electrospinning parameters on the wettability of the PS/ Al_2O_3 nanocomposite is investigated. Table 3 reveals the measured values of WCA and SA for both PS and PS/ Al_2O_3 nanocomposite coatings using the sessile droplet method at ambient temperature.

Table 3. WCA and CAH of the prepared PS and PS/Al₂O₃ nanocomposite coatings.

Code	WCA	WCAH
PS1	141° ± 2°	24° ± 3°
PS2	143° ± 3°	20° ± 4°
PS3	147° ± 1°	14° ± 3°
PS4	138° ± 2°	32° ± 6°
PA1	151° ± 2.8°	7° ± 2.3°
PA2	152° ± 1.2°	5° ± 3.1°
PA3	155° ± 1.9°	3° ± 4.2°
PA4	147° ± 2°	13° ± 3°

Figure 4 shows snapshots for the measured WCA after and before the addition of Al₂O₃ nanoparticles. The WCA of the uncoated Al substrate was around 87° ± 2.2°. However, WCAs values of the PS coatings vary with the processing parameters of electrospinning, due to the variation of the fibers diameters. The highest WCA and lowest CAH of the PS-coated materials is 147° ± 1° and 14° ± 3°, respectively, for PS3, which is formed at a flow rate of 1.5 mL·h⁻¹ and an applied voltage of 25 kV. Nevertheless, the addition of Al₂O₃ nanoparticles to PS polymer improved the hydrophobicity of the nanocomposite coating. The highest WCA and lowest CAH average values are 155.2° ± 1.9° and 3° ± 4.2°, respectively, for PA3.

**Figure 4.** Snapshots of the measured water contact angle after and before the addition of Al₂O₃ nanoparticles.

The static contact angle is measured according to the Wenzel and Cassie–Baxter models. The hypothesis developed by Wenzel is described in Equation (1) [47,48].

$$\cos \theta^* = r \cos \theta_Y \quad (1)$$

in which r is the ratio between the true surface area and the apparent one (for a rough surface $r > 1$ and =1 for a smooth one). θ^* is the apparent macroscopic WCA and θ_Y is the intrinsic contact angle for the droplet on a corresponding flat surface obtained by the Young's equation (as defined for an ideal surface). On the other hand, Cassie–Baxter regime suggested that the water droplet is suspended on the rough surfaces and is not penetrated into the channels among the rough surface, resulting in

heterogeneous structures consisting of air and solids. Therefore, the contact angle in terms of the Cassie-Baxter hypothesis is given in Equation (2) [49]:

$$\cos \theta_{CB} = r_f f_1 \cos \theta_Y - f_2 \quad (2)$$

in which θ_{CB} and θ_Y represent the contact angle on the rough nanocomposite coating (PS/Al₂O₃) and the smooth PS surfaces, respectively. f_1 and f_2 are the area fractions of the solid and air on the surface in which $f_1 + f_2 = 1$. Given that θ_{CB} is $151^\circ \pm 2.8^\circ$, $152^\circ \pm 1.2^\circ$ and $155^\circ \pm 1.9^\circ$ for PA1, PA2, and PA3 nanocomposite coatings, respectively, and θ_Y for the PS before addition of Al₂O₃ equals $141^\circ \pm 2^\circ$, $143^\circ \pm 3^\circ$, and $147^\circ \pm 1^\circ$ for PS1, PS2, and PS3, respectively, then the estimated values of f_2 are 0.43, 0.42, and 0.47, respectively. These calculations indicate that air occupies about 43%, 42%, and 47% of the contact regions area for the as-prepared PA1, PA2, and PA3 nanocomposite coating, respectively. This confirms that the reason behind the superhydrophobicity of the PS/Al₂O₃ composite coating is mainly attributed to the multiscale (hierarchical) roughness of the surface, which is induced by the micro-/nano-sized fibers or beads and the nanoparticles incorporated in the polymer solution.

CAH is an important parameter to be measured besides the WCA, as it gives information about the stickiness of the surface. The high WCA of the coating does not necessarily indicate a low CAH, due to the effect of chemical heterogeneity [50]. The CAHs of PS coatings before the addition of Al₂O₃ nanoparticles are $24^\circ \pm 3^\circ$, $20^\circ \pm 4^\circ$, $14^\circ \pm 3^\circ$, and $32^\circ \pm 6^\circ$ for PS1, PS2, PS3, and PS4 respectively, as shown in Table 3. The increase of the nanofiber diameter at high PS concentration showed a low WCA and a high CAH for PS4. After the addition of Al₂O₃ nanoparticles, the CAH decreased to 7.1 ± 2.3 , 5 ± 3.1 , and 3 ± 4.2 for PA1, PA2, and PA3, respectively. These results reveal a low adhesion force between the prepared PS/Al₂O₃ nanocomposite surface and water droplets, which allows water droplets to slide easily from the substrate's surface.

In addition to the thickness of the fiber and the electrospinning parameters, the size of the nanoparticles may have an effect on the wettability. According to Conti et al. [51], a combination of silica nanoparticles of two different sizes (70 and 100 nm) increased the WCA to 147° and lowered the WCAH to 10° . However, when the size of SiO₂ nanoparticles was increased to 150 nm, the WCA was decreased drastically to 124° . On the other hand, Karapanagiotis et al. [52] used Al₂O₃ nanoparticles with different sizes (25, 35, and 150 nm) in their coatings, and they found that the coating wettability is independent of the size of the nanoparticles. Then, in a more recent study, they [53] found an effect for the size of the nanoparticles on the wettability of their coatings, only if the concentration of the nanoparticle is high.

Figure 5 shows the FTIR spectra of pure PS and PS/Al₂O₃ nanocomposite coatings at different electrospinning parameters and concentrations of PS and Al₂O₃. The spectra for PS before and after the addition of Al₂O₃ with different electrospinning parameters are very similar. No remarkable changes are observed before and after addition of Al₂O₃. This is probably because of the small concentration of the Al₂O₃ used compared with the PS amount. The FTIR of Al₂O₃, Figure 5a, shows a transmission band located at about 3400 cm^{-1} that is assigned to hydrogen-bonded -O-H of the adsorbed water, while the band at $400\text{--}1000 \text{ cm}^{-1}$ can be attributed to the bending stretching band of Al-O [54]. PS/Al₂O₃ nanocomposite and PS show the same spectra between the $700\text{--}3100 \text{ cm}^{-1}$. Bands of the IR spectrum for PS correspond to their functional groups. The observed peaks at $3000\text{--}3100 \text{ cm}^{-1}$ are attributed to the aromatic C-H stretching vibration and the C-H group on the PS side chain. However, the absorbance bands at 2922 and 2854 cm^{-1} correspond to the C-H stretching vibration of the -CH₂ and -CH groups on the main PS chain. The C-C aromatic stretch and the vibration of the aromatic ring are noticed at 1494 and 1091 cm^{-1} , respectively. The strong peaks located at 700 and 760 cm^{-1} are ascribed to -CH₂ rocking mode and C-H out-of-plane bend, respectively. The inorganic segment of the Al-O-Al band can be noticed at $400\text{--}800 \text{ cm}^{-1}$, and its absorbance intensity increases with increasing the Al₂O₃ content [55]. However, it is noticed that there no new bands appear after adding Al₂O₃ nanoparticles to the PS, which proves that (i) Al₂O₃ only interacted physically with PS [56], and (ii) the electrospinning in this case does not affect the chemical structure of the polymer.

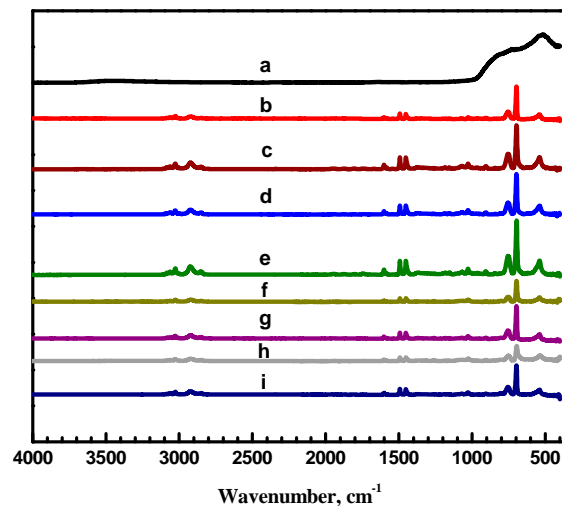


Figure 5. FTIR for (a) Al₂O₃ nanoparticles, (b) PS1, (c) PS2, (d) PS3, (e) PS4, (f) PA1, (g) PA2, (h) PA3, and (i) PA4.

To better understand the effect of nanoparticle addition on PS, AFM is used to document the surface topography of both PS and PS/Al₂O₃ nanocomposite coatings. AFM images in Figure 6 and Table 4 show the 3D height and the roughness values (R_a), respectively. It is clear from Table 4 that the R_a of the prepared PS coatings before the addition of the Al₂O₃ nanoparticles (PS1, PS2, PS3, and PS4) are slightly close to each other. In the images a–d of Figure 6, it can be noticed that the PS surface is relatively smooth and small bumps appeared on the surface, which may happen due to the beaded fibers structure. However, after the addition of Al₂O₃ nanoparticles, the R_a values significantly increase as shown in Table 4 and in Images e–h in Figure 6.

Table 4. The R_a values of PS and PS/Al₂O₃ nanocomposite coatings.

Codes	R_a Values (nm)
PS1	22 ± 2
PS2	26 ± 4
PS3	32 ± 3
PS4	17 ± 4
PA1	53 ± 3
PA2	61 ± 4
PA3	82 ± 2
PA4	27 ± 3

The R_a values of PS1, PS2, PS3, and PS4 before the addition of the Al₂O₃ nanoparticles are 22 ± 2 , 26 ± 4 , 32 ± 3 , and 17 ± 4 nm, respectively. However after the addition of the nanoparticles, the surface roughness values increases to 53 ± 3 , 61 ± 4 , 82 ± 2 , and 27 ± 3 nm for PA1, PA2, PA3, and PA4, respectively. This explains why PA3 has the highest WCAs. The AFM measurements verified the effect of the composition ratio and the electrospinning operational parameters on the surface roughness of superhydrophobic nanocomposite coatings. Generally, Al₂O₃ and the combination of micro beads/nano fiber structure increase the roughness, which in turn increases the WCA in comparison with the pure PS polymer. It also can be noticed that increasing the concentration of PS or the flow rate decreases the surface roughness and consequently lowers the WCA. It is worth mentioning that lowering the operational potential from 25 to 20 kV also decreases the surface roughness and consequently lowers the WCA.

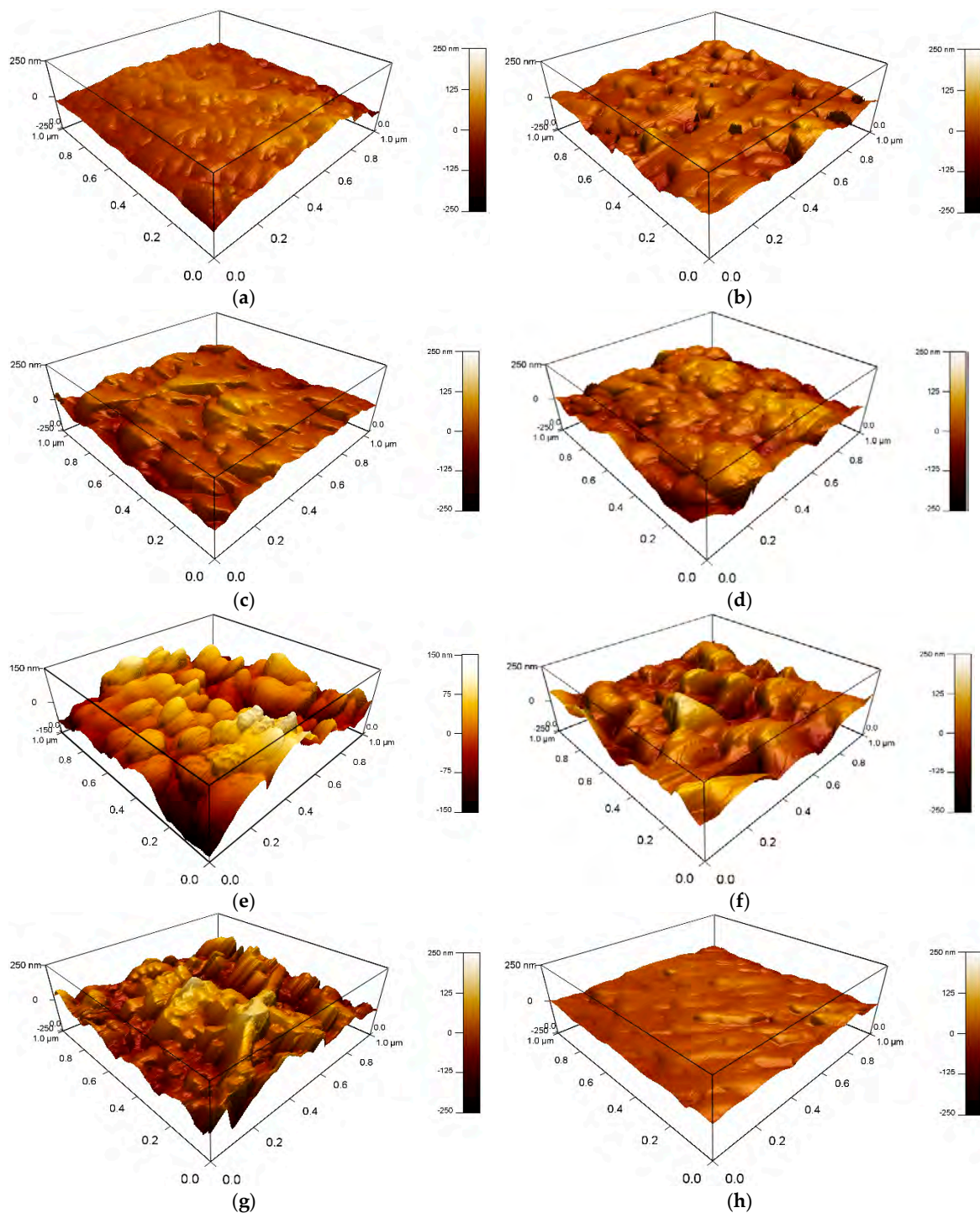


Figure 6. AFM 3D images for (a) PS1, (b) PS2, (c) PS3, (d) PS4, (e) PA1, (f) PA2, (g) PA3, and (h) PA4.

3.3. Anticorrosion Performance of the As-Prepared Nanocomposite Coatings

As a non-destructive technique, EIS is usually used to study the corrosion mechanism and the corrosion resistance of SHCs. Figures 7 and 8 show the Nyquist and Bode plots of the measured EIS data, respectively. The dots are the measured data, while the solid lines are the fitted data using the electrical equivalent circuit shown in Figure 9 that has two time constants. R_{p0} and R_{ct} refer to the coating pore resistance and charge transfer resistance, respectively. On the other hand, C_{dl1} and C_{dl2} are the double layer capacitances of the constant phase elements representing the coating/solution and

metal/solution interfaces, respectively. The high-frequency intercept $|Z_{100} \text{ kHz}|$ refers to the solution resistance (R_s), and the low-frequency intercept $|Z_{0.01} \text{ Hz}|$ represents the sum of the solution and charge transfer resistances. Simply, the larger the diameter of the semicircle (charge transfer resistance), the lower the corrosion rate is. Table 5 exhibits the fitted data that were attained from Gamry Echem Analyst software. The capacitances are substituted by constant phase elements (C_{dl1} and C_{dl2}) to give a more precise fit to the experimental outcomes. The exponent ($0 \leq n \leq 1$) represents deviation from an ideal dielectric behavior; if $n = 0$, it shows an ideal resistor, and if $n = 1$, it acts as an ideal capacitor [57–64]. It is noticed that the R_{po} and R_{ct} significantly increase as the WCA increases. Increasing the WCA form $141^\circ \pm 2^\circ$ to $147^\circ \pm 1^\circ$ of the hydrophobic coatings has a significant influence on increasing the R_{ct} from $102 \text{ k}\Omega \cdot \text{cm}^2$ of PS1 to $140 \text{ k}\Omega \cdot \text{cm}^2$ of PS3. However, increasing the WCA to $151^\circ \pm 2.8^\circ$ and $155^\circ \pm 1.9^\circ$ and decreasing the CAH to 7 ± 2.3 and 3 ± 4.2 leads to a remarkable increase of the R_{ct} to three orders of magnitude (8 and $18 \times 10^6 \text{ k}\Omega \cdot \text{cm}^2$) in comparison to the uncoated Al, respectively. On the other hand, C_{dl1} and C_{dl2} of the SHCs distinctly is decreased to very low values in comparison to the uncoated and PS-coated Al substrates (PS1 and PS3), which indicates a low permeation of the electrolyte to the SHC/metal surface and a polarization resistance. It is worth mentioning that the shape of the phase angle of the uncoated and the coated Al (see Figure 8a,c), is not changed, which could be ascribed to the electrolyte permeation through the coating defects. The high corrosion resistance of the as prepared SHCs can be attributed to the trapped air in the disproportions of the heterogeneous surface, which prevents the aggressive ions from easily attacking the underlying surface of Al alloy. Moreover, the hydrophobic PS is non-polar and very good electrical insulator; therefore, aggressive ions can hardly transport through such coatings and reach the metal surface, thereby showing a superior corrosion resistance via physical modification of its surface.

Table 5. The electrochemical parameters from Nyquist and Bode plots for the uncoated and coated aluminum substrates with pure electrospun PS (PS1 & PS3), and nanocomposite SHCs of polystyrene and aluminum oxide (PA1 & PA3), in 3.5 wt % NaCl solution.

Samples	WCA ($^\circ$)	R_{po} ($\text{k}\Omega \cdot \text{cm}^2$)	R_{ct} ($\text{k}\Omega \cdot \text{cm}^2$)	Y_{01} ($\Omega^{-1} \cdot \text{cm}^{-2} \cdot \text{s}^n$) $\times 10^{-6}$	n_1	C_{dl1} ($\mu\text{F} \cdot \text{cm}^{-2}$)	Y_{02} ($\Omega^{-1} \cdot \text{cm}^{-2} \cdot \text{s}^n$) $\times 10^{-6}$	n_2	C_{dl2} ($\mu\text{F} \cdot \text{cm}^{-2}$)
uncoated Al alloy	87 ± 2	0.7	4	1100	0.833	1500	148	0.763	120
PS1	141 ± 2	77	102	28	0.735	41	4	0.701	2.7
PS3	147 ± 1	220	140	8	0.714	8.3	1.8	0.697	0.98
PA1	151 ± 2.8	530	8000	0.048	0.692	0.033	0.004	0.408	3.4×10^{-5}
PA3	155 ± 1.9	860	18000	0.013	0.585	0.0047	0.0012	0.263	2.5×10^{-8}

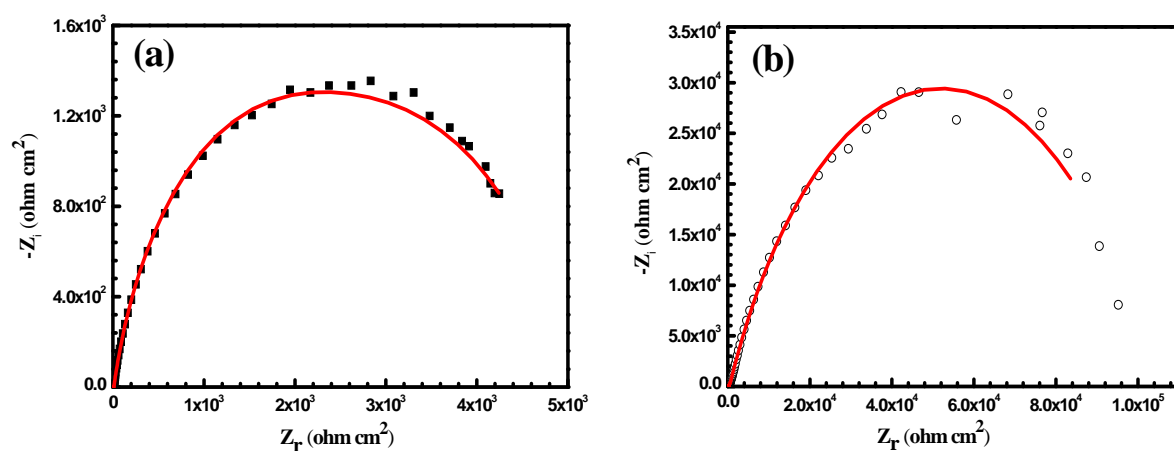


Figure 7. Cont.

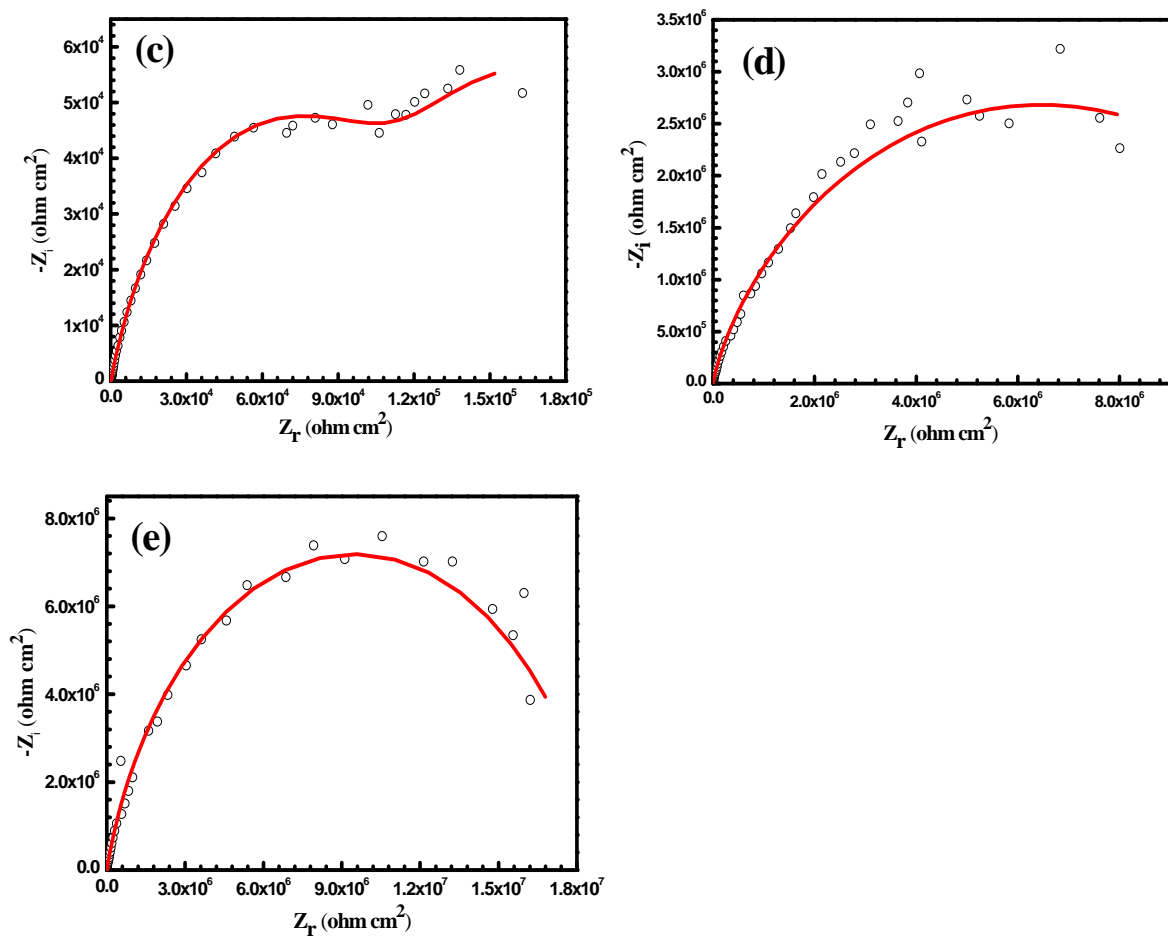


Figure 7. Nyquist plots of the (a) uncoated Al alloy (b) PS1, (c) PS3, (d) PA1, and (e) PA3 from the EIS measurements in 3.5 wt % NaCl.

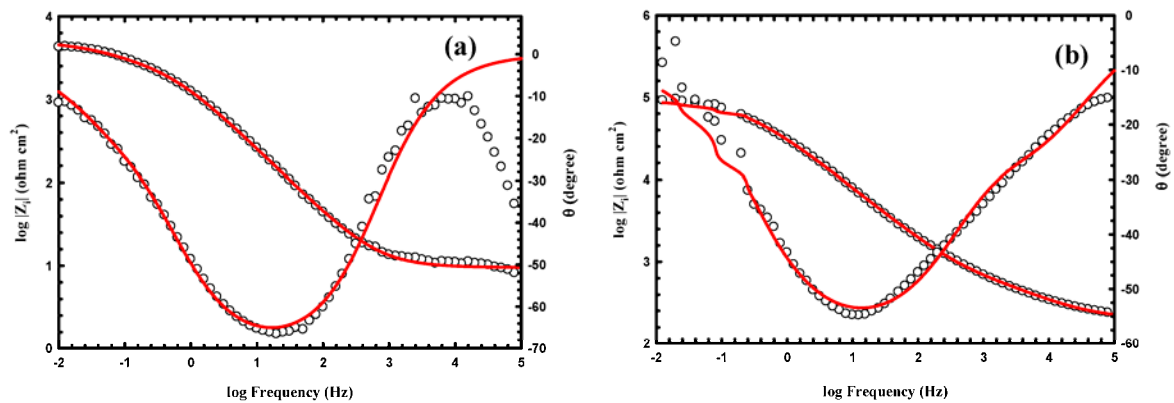


Figure 8. Cont.

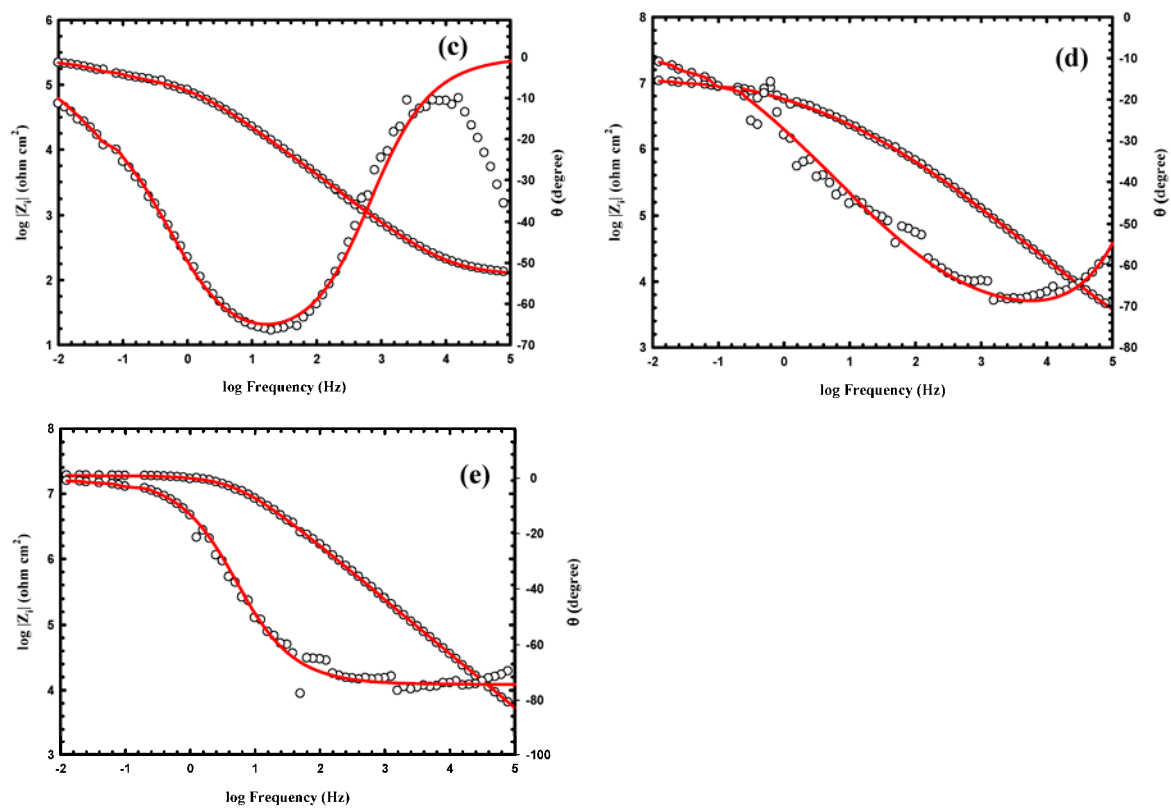


Figure 8. Bode plots of the (a) uncoated Al alloy (b) PS1, (c) PS3, (d) PA1, and (e) PA3 from the EIS measurements in 3.5 wt % NaCl.

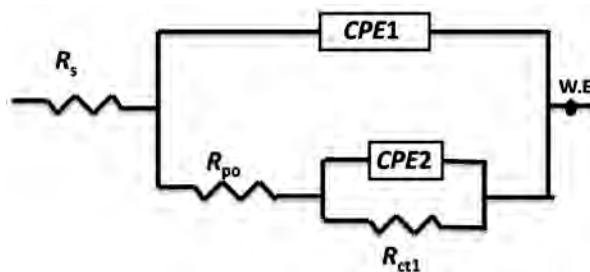


Figure 9. Equivalent electrical circuit used to fit the EIS spectra of the uncoated Al alloy and the as-prepared SHCs in saline water.

4. Conclusions

The different electrospinning operational parameters have a great influence on the morphology, surface roughness, and wettability of the pure PS and PS/Al₂O₃ nanocomposite coatings. Also, the addition of Al₂O₃ nanoparticles markedly increases the surface roughness. The highest WCA is measured for the nanocomposite PA3 (which has the highest surface roughness with an R_a of 82 ± 2 nm) and was found to be $155^\circ \pm 1.9^\circ$. On the other hand, increasing the PS concentration is not recommended to increase the WCA. In addition, it is revealed that increasing the nanofiber diameter decreases the WCA and increases the CAH. The optimum conditions of electrospinning in order to obtain the highest possible water contact angle ($155^\circ \pm 1.9^\circ$), and low sliding angle 3 ± 4.2 , are a flow rate of $1.5 \text{ mL}\cdot\text{h}^{-1}$ and an applied voltage of 25 kV with polystyrene: an Al₂O₃ ratio of 1:10. In addition, the higher the WCA, the higher the corrosion resistance and the lower WCAH are. The combination of the micro-nano structure of the beaded fiber morphology results in high WCA and

low WCAH. Despite their highly porous nature, the as-synthesized SHCs (PA1 & PA3) significantly increased the corrosion resistance of Al in saline water more than three orders of magnitude.

Acknowledgments: This publication was supported by Qatar University Internal Grant No. GCC-2017-012. The findings achieved herein are solely the responsibility of the authors. Thanks are also due to Anton Popelka for assistance with the AFM analysis.

Author Contributions: Ahmed Bahgat Radwan performed all the experiments and helped write some parts of the manuscript. Aboubakr M. Abdullah designed the whole corrosion work besides some of the superhydrophobic work, wrote parts of the manuscript, and reviewed it as a whole. Adel M. A. Mohamed designed most of the superhydrophobic work, was involved in all of the discussions, and helped write the manuscript. Mariam A. Al-Maadeed was responsible for the coating characterization.

Conflicts of Interest: The author declares no conflict of interest.

References

1. Nakajima, A.; Fujishima, A.; Hashimoto, K.; Watanabe, T. Preparation of transparent superhydrophobic boehmite and silica films by sublimation of aluminum acetylacetonate. *Adv. Mater.* **1999**, *11*, 1365–1368. [[CrossRef](#)]
2. Schindelholz, E.; Kelly Robert, G. Wetting phenomena and time of wetness in atmospheric corrosion: A review. *Corros. Rev.* **2012**, *30*, 135–170. [[CrossRef](#)]
3. Bhushan, B.; Jung, Y.C.; Koch, K. Self-cleaning efficiency of artificial superhydrophobic surfaces. *Langmuir* **2009**, *25*, 3240–3248. [[CrossRef](#)] [[PubMed](#)]
4. Sun, T.; Tan, H.; Han, D.; Fu, Q.; Jiang, L. No platelet can adhere—Largely improved blood compatibility on nanostructured superhydrophobic surfaces. *Small* **2005**, *1*, 959–963. [[CrossRef](#)] [[PubMed](#)]
5. Ishizaki, T.; Saito, N. Rapid formation of a superhydrophobic surface on a magnesium alloy coated with a cerium oxide film by a simple immersion process at room temperature and its chemical stability. *Langmuir* **2010**, *26*, 9749–9755. [[CrossRef](#)] [[PubMed](#)]
6. Jin, S.; Choi, C. Superhydrophobic and Superoleophobic Nano Surfaces Used as Antifingerprint Touch Sensitive Screen. WO Patent Application No. 2012087352A2, 28 June 2012.
7. Zhang, L.; Wu, J.; Hedhili, M.N.; Yang, X.; Wang, P. Inkjet printing for direct micropatterning of a superhydrophobic surface: Toward biomimetic fog harvesting surfaces. *J. Mater. Chem. A* **2015**, *3*, 2844–2852. [[CrossRef](#)]
8. Zhou, Z.; Fa, W.X. Electrospinning superhydrophobic-superoleophilic fibrous PVDF membranes for high-efficiency water-oil separation. *Mater. Lett.* **2015**, *160*, 423–427. [[CrossRef](#)]
9. Lapierre, F.; Harnois, M.; Coffinier, Y.; Boukherroub, R.; Thomy, V. Split and flow: Reconfigurable capillary connection for digital microfluidic devices. *Lab Chip* **2014**, *14*, 3589–3593. [[CrossRef](#)] [[PubMed](#)]
10. Ivanova, E.P.; Hasan, J.; Webb, H.K.; Truong, V.K.; Watson, G.S.; Watson, J.A.; Baulin, V.A.; Pogodin, S.; Wang, J.Y.; Tobin, M.J.; et al. Natural bactericidal surfaces: Mechanical rupture of pseudomonas aeruginosa cells by cicada wings. *Small* **2012**, *8*, 2489–2494. [[CrossRef](#)] [[PubMed](#)]
11. Gao, X.; Jiang, L. Biophysics: Water-repellent legs of water striders. *Nature* **2004**, *432*, 36. [[CrossRef](#)] [[PubMed](#)]
12. Hu, D.L.; Bush, J.W.M. Meniscus-climbing insects. *Nature* **2005**, *437*, 733–736. [[CrossRef](#)] [[PubMed](#)]
13. Liu, K.; Du, J.; Wu, J.; Jiang, L. Superhydrophobic gecko feet with high adhesive forces towards water and their bio-inspired materials. *Nanoscale* **2012**, *4*, 768–772. [[CrossRef](#)] [[PubMed](#)]
14. Min, W.L.; Jiang, B.; Jiang, P. Bioinspired self-cleaning antireflection coatings. *Adv. Mater.* **2008**, *20*, 3914–3918. [[CrossRef](#)]
15. Bayer, I. On the durability and wear resistance of transparent superhydrophobic coatings. *Coatings* **2017**, *7*, 12. [[CrossRef](#)]
16. Heib, F.; Schmitt, M. Statistical contact angle analyses with the high-precision drop shape analysis (HPDSA) approach: Basic principles and applications. *Coatings* **2016**, *6*, 57. [[CrossRef](#)]
17. Lee, K.-M.; Ngo, C.V.; Jeong, J.Y.; Jeon, E.-C.; Je, T.J.; Chun, D.M. Fabrication of an anisotropic superhydrophobic polymer surface using compression molding and dip coating. *Coatings* **2017**, *7*, 194. [[CrossRef](#)]
18. Fontananova, E.; Jansen, J.C.; Cristiano, A.; Curcio, E.; Drioli, E. Effect of additives in the casting solution on the formation of pvdf membranes. *Desalination* **2006**, *192*, 190–197. [[CrossRef](#)]

19. Anton, F. Process and Apparatus for Preparing Artificial Threads. U.S. Patent Application No. 1975504A, 2 October 1934.
20. Huang, Z.M.; Zhang, Y.Z.; Kotaki, M.; Ramakrishna, S. A review on polymer nanofibers by electrospinning and their applications in nanocomposites. *Compos. Sci. Technol.* **2003**, *63*, 2223–2253. [[CrossRef](#)]
21. Deitzel, J.M.; Kleinmeyer, J.; Harris, D.; Beck Tan, N.C. The effect of processing variables on the morphology of electrospun nanofibers and textiles. *Polymer* **2001**, *42*, 261–272. [[CrossRef](#)]
22. Sukigara, S.; Gandhi, M.; Ayutsede, J.; Micklus, M.; Ko, F. Regeneration of bombyx mori silk by electrospinning—Part 1: Processing parameters and geometric properties. *Polymer* **2003**, *44*, 5721–5727. [[CrossRef](#)]
23. Demir, M.M.; Yilgor, I.; Yilgor, E.; Erman, B. Electrospinning of polyurethane fibers. *Polymer* **2002**, *43*, 3303–3309. [[CrossRef](#)]
24. Fong, H.; Chun, I.; Reneker, D.H. Beaded nanofibers formed during electrospinning. *Polymer* **1999**, *40*, 4585–4592. [[CrossRef](#)]
25. Ondarçuhu, T.; Joachim, C. Drawing a single nanofibre over hundreds of microns. *Europhys. Lett.* **1998**, *42*, 215. [[CrossRef](#)]
26. Feng, L.; Li, S.; Li, H.; Zhai, J.; Song, Y.; Jiang, L.; Zhu, D. Super-hydrophobic surface of aligned polyacrylonitrile nanofibers. *Angew. Chem. Int. Ed.* **2002**, *41*, 1221–1223. [[CrossRef](#)]
27. Ma, P.X.; Zhang, R. Synthetic nano-scale fibrous extracellular matrix. *J. Biomed. Mater. Res.* **1999**, *46*, 60–72. [[CrossRef](#)]
28. Liu, G.; Qiao, L.; Guo, A. Diblock copolymer nanofibers. *Macromolecules* **1996**, *29*, 5508–5510. [[CrossRef](#)]
29. Doshi, J.; Reneker, D.H. Electrospinning process and applications of electrospun fibers. *J. Electrostat.* **1995**, *35*, 151–160. [[CrossRef](#)]
30. Mohamed, M.A.; Abdullah, A.B.; Al-Maadeed, M.; Radwan, A.B. Fundamental, fabrication and applications of superhydrophobic surfaces fabrication and applications of superhydrophobic surfaces. In *Research Perspectives on Functional Micro-and Nanoscale Coatings*; Zuzuarregui, A., Morant-Miñana, M.C., Eds.; IGI Global: Hershey, PA, USA, 2016; pp. 341–368.
31. Radwan, A.B.; Abdullah, A.B.; Alnuaimi, N.A. Recent advances in corrosion resistant superhydrophobic coatings. *Corros. Rev.* **2017**. [[CrossRef](#)]
32. Lee, K.H.; Kim, H.Y.; Bang, H.J.; Jung, Y.H.; Lee, S.G. The change of bead morphology formed on electrospun polystyrene fibers. *Polymer* **2003**, *44*, 4029–4034. [[CrossRef](#)]
33. Maul, J.; Frushour, B.G.; Kontoff, J.R.; Eichenauer, H.; Ott, K.H.; Schade, C. Polystyrene and styrene copolymers. In *Ullmann's Encyclopedia of Industrial Chemistry*; Wiley-VCH Verlag GmbH & Co. KGaA: Weinheim, Germany, 2000.
34. Jarusuwannapoom, T.; Hongrojjanawiwat, W.; Jitjaicham, S.; Wannatong, L.; Nithitanakul, M.; Pattamaprom, C.; Koombhongse, P.; Rangkupan, R.; Supaphol, P. Effect of solvents on electro-spinnability of polystyrene solutions and morphological appearance of resulting electrospun polystyrene fibers. *Eur. Polym. J.* **2005**, *41*, 409–421. [[CrossRef](#)]
35. Acatay, K.; Simsek, E.; Ow-Yang, C.; Menciloglu, Y.Z. Tunable, superhydrophobically stable polymeric surfaces by electrospinning. *Angew. Chem. Int. Ed.* **2004**, *116*, 5322–5325. [[CrossRef](#)]
36. Hou, W.; Wang, Q. Wetting behavior of a SiO₂-polystyrene nanocomposite surface. *J. Colloid Interface Sci.* **2007**, *316*, 206–209. [[CrossRef](#)] [[PubMed](#)]
37. Hou, W.; Wang, Q. UV-driven reversible switching of a polystyrene/titania nanocomposite coating between superhydrophobicity and superhydrophilicity. *Langmuir* **2009**, *25*, 6875–6879. [[CrossRef](#)] [[PubMed](#)]
38. Xu, X.; Zhang, Z.; Guo, F.; Yang, J.; Zhu, X.; Zhou, X.; Xue, Q. Fabrication of bionic superhydrophobic manganese oxide/polystyrene nanocomposite coating. *J. Bionic Eng.* **2012**, *9*, 11–17. [[CrossRef](#)]
39. Wang, Y.; Li, B.; Liu, T.; Xu, C.; Ge, Z. Controllable fabrication of superhydrophobic TiO₂ coating with improved transparency and thermostability. *Colloids Surf. A* **2014**, *441*, 298–305. [[CrossRef](#)]
40. Hart, L.D. *Alumina Chemicals: Science and Technology Handbook*; American Ceramic Society: Columbus, OH, USA, 1990.
41. Keyvani, A.; Saremi, M.; Heydarzadeh Sohi, M. Microstructural stability of zirconia–alumina composite coatings during hot corrosion test at 1050 °C. *J. Alloys Compd.* **2010**, *506*, 103–108. [[CrossRef](#)]

42. Zhan, N.; Li, Y.; Zhang, C.; Song, Y.; Wang, H.; Sun, L.; Yang, Q.; Hong, X. A novel multinozzle electrospinning process for preparing superhydrophobic PS films with controllable bead-on-string/microfiber morphology. *J. Colloid Interface Sci.* **2010**, *345*, 491–495. [[CrossRef](#)] [[PubMed](#)]
43. Lee, J.S.; Choi, K.H.; Ghim, H.D.; Kim, S.S.; Chun, D.H.; Kim, H.Y.; Lyoo, W.S. Role of molecular weight of atactic poly(vinyl alcohol) (PVA) in the structure and properties of PVA nanofabric prepared by electrospinning. *J. Appl. Polym. Sci.* **2004**, *93*, 1638–1646. [[CrossRef](#)]
44. Megelski, S.; Stephens, J.S.; Chase, D.B.; Rabolt, J.F. Micro- and nanostructured surface morphology on electrospun polymer fibers. *Macromolecules* **2002**, *35*, 8456–8466. [[CrossRef](#)]
45. Baumgarten, P.K. Electrostatic spinning of acrylic microfibers. *J. Colloid Interface Sci.* **1971**, *36*, 71–79. [[CrossRef](#)]
46. Kim, E.S.; Kim, S.H.; Lee, C.H. Electrospinning of polylactide fibers containing silver nanoparticles. *Macromol. Res.* **2010**, *45*, 215–221. [[CrossRef](#)]
47. Tuberquia, J.C.; Nizamidin, N.; Robert, R.; Harl, R.R.; Albert, J.; Hunter, J.; Rogers, B.R.; Kane, G.J. Surface-Initiated Polymerization of Superhydrophobic Polymethylene. *J. Am. Chem. Soc.* **2010**, *132*, 5725–5734. [[CrossRef](#)] [[PubMed](#)]
48. Wenzel, R.N. Resistance of solid surfaces to wetting by water. *Ind. Eng. Chem.* **1936**, *28*, 988–994. [[CrossRef](#)]
49. Cassie, A.B.D.; Baxter, S. Wettability of porous surfaces. *Trans. Faraday Soc.* **1944**, *40*, 546–551. [[CrossRef](#)]
50. Quere, D. Surface chemistry: Fakir droplets. *Nat. Mater.* **2002**, *1*, 14–15. [[CrossRef](#)] [[PubMed](#)]
51. Conti, J.; De Coninck, J.; Ghazzal, M.N. Design of water-repellant coating using dual scale size of hybrid silica nanoparticles on polymer surface. *Appl. Surf. Sci.* **2018**, *436*, 234–241. [[CrossRef](#)]
52. Karapanagiotis, I.; Manoudis, P.N.; Savva, A.; Panayiotou, C. Superhydrophobic polymer-particle composite films produced using various particle sizes. *Surf. Interface Anal.* **2012**, *44*, 870–875. [[CrossRef](#)]
53. Manoudis, P.N.; Karapanagiotis, I. Modification of the wettability of polymer surfaces using nanoparticles. *Prog. Org. Coat.* **2014**, *77*, 331–338. [[CrossRef](#)]
54. Wang, Y.; Suryanarayana, C.; An, L. Phase transformation in nanometer-sized γ -alumina by mechanical milling. *J. Am. Ceram. Soc.* **2005**, *88*, 780–783. [[CrossRef](#)]
55. Ghezelbash, Z.; Ashouri, D.; Mousavian, S.; Ghandi, A.H.; Rahnama, Y. Surface modified Al_2O_3 in fluorinated polyimide/ Al_2O_3 nanocomposites: Synthesis and characterization. *Bull. Mater. Sci.* **2012**, *35*, 925–931. [[CrossRef](#)]
56. Radwan, A.B.; Mohamed, A.M.A.; Abdullah, A.M.; Al-Maadeed, M.A. Corrosion protection of electrospun pvdF-ZnO superhydrophobic coating. *Surf. Coat. Technol.* **2016**, *289*, 136–143. [[CrossRef](#)]
57. Tang, C.; Stueber, M.; Seifert Hans, J.; Steinbrueck, M. Protective coatings on zirconium-based alloys as accident-tolerant fuel (ATF) claddings. *Corros. Rev.* **2017**, *35*, 141–165. [[CrossRef](#)]
58. Kadappambil, S.; Yadav, K.; Ramachandran, M.; Victoria Selvam, N. Electrochemical investigation of the corrosion inhibition mechanism of tectona grandis leaf extract for SS304 stainless steel in hydrochloric acid. *Corros. Rev.* **2017**, *35*, 111–121. [[CrossRef](#)]
59. Kumar, R.; Chahal, S.; Dahiya, S.; Dahiya, N.; Kumar, S.; Lata, S. Experimental and theoretical approach to exploit the corrosion inhibition activity of 3-formyl chromone derivatives on mild steel in 1 M H_2SO_4 . *Corros. Rev.* **2017**, *35*, 95–110. [[CrossRef](#)]
60. Dahiya, S.; Lata, S.; Kumar, P.; Kumar, R. A descriptive study for corrosion control of low-alloy steel by aloe vera extract in acidic medium. *Corros. Rev.* **2016**, *34*, 241–248. [[CrossRef](#)]
61. Fayyad, E.; Abdullah, A.; Hassan, M.; Mohamed, A.; Wang, C.; Jarjoura, G.; Farhat, Z. Synthesis, characterization, and application of novel Ni-P-carbon nitride nanocomposites. *Coatings* **2018**, *8*, 37. [[CrossRef](#)]
62. Bai, Y.; Xing, J.; Guo, Y.; Li, J.; Huang, Q.; Gao, Y. Influence of 4 wt % Cr addition on the corrosion-wear synergistic effect for $\text{Al}_2\text{O}_3/\text{Fe}(\text{Al})$ composites. *Corros. Rev.* **2016**, *34*, 231–240. [[CrossRef](#)]
63. Książek, M. Resistance to chemical attack of cement composites impregnated with a special polymer sulfur composite. *Corros. Rev.* **2016**, *34*, 211–229. [[CrossRef](#)]
64. Yang, D.; Liu, S.H.; Shao, Y.P.; Di Xu, S.; Zhao, L.L.; Liao, Q.Q.; Ge, H.H. Electrochemical and XPS studies of alkyl imidazoline on the corrosion inhibition of carbon steel in citric acid solution. *Corros. Rev.* **2016**, *34*, 295–304. [[CrossRef](#)]

